

TURBULENCE MODELS FOR AMPHIBIOUS AIRCRAFT WITH CFD AND WIND TUNNEL

Karyawan, K.*; Suwasono, B.**.#; Hasim, F.*; Yohana, E.***; Rossel, G.*** & Haryanto, I.***

* Research Centre for Aeronautics Technology, National Research and Innovation Agency, Rumpin 160350, Indonesia

** Graduate Programme of Marine Technology, University of Hang Tuah, Surabaya 60111, Indonesia

*** Department of Mechanical Engineering, University of Diponegoro, Semarang 50275, Indonesia

E-Mail: karyo01@brin.go.id, bagiyo.suwasono@hangtuah.ac.id, fadilah.hasim@brin.go.id, eflitayohana@live.undip.ac.id, glayenrossel@alumni.undip.ac.id, ismoyoharyanto@lecturer.undip.ac.id (# Corresponding author)

Abstract

Indonesia is an archipelagic country that significantly depends on ships to connect several islands. However, these ships are considered to lack speed and flexibility, leading to the use of amphibious aircraft as an alternative to ships. The development of amphibious aircraft heavily relies on aerodynamic analysis, especially the turbulence model. The turbulence modelling methods that were analysed included K-Omega SST, K-Epsilon, and Spalart-Allmaras. The best turbulence model from the results of computing and C_L/C_D calculating for the amphibious aircraft model without a propeller has the Spalart-Allmaras model with a lower value, and the error results are less than 5.05 %.

(Received in December 2025, accepted in May 2026. This paper was with the authors 2 months for 1 revision.)

Key Words: K-Omega SST, K-Epsilon, Spalart-Allmaras, Lift Coefficient, Drag Coefficient

1. INTRODUCTION

Indonesia is an archipelagic country characterized by various islands, creating challenges in terms of communication and coordination. Therefore, sea and air transportation play a significant role for inter-island connectivity [1]. Most of the transportation used are ships, which can accommodate many passengers and cargo. Although ships can connect islands, there is limitation regarding time and speed, leading to less suitability for emergencies requiring fast and flexible transportation [2]. To address this limitation, aircraft offers alternative advantages, providing speed and system flexibility. The widespread use of aircraft is restricted by insufficient infrastructure, as not all islands have enough land to build airports. Generally, commercial aircraft requires a minimum runway length of 1500 meters, which is not feasible in small land area. In response to the challenge, amphibious aircraft with Short Take Off Landing (STOL) capabilities, which can take off and land within a short distance of approximately 150 meters, offers promising solution. Amphibious aircraft can also land on water, making their development strategically valuable for areas without conventional landing facilities or runways. This provides a practical solution due to the ability to take off and landing from both land and water surfaces, eliminating the need for airport construction for landing [3].

The amphibious aircraft is influenced by aerodynamic coefficients, engine thrust, and hydrodynamic coefficients [4]. Several aircraft motion parameters that need to be considered include drag, flight speed, and pitch angle, which change over time, affecting both hydrodynamic and aerodynamic coefficients [5]. Computational Fluid Dynamics (CFD) is used as a tool to study aerodynamic characteristics by analysing pressure distribution and separation areas, providing better flow visualization [6]. In CFD, the selection of a turbulence model is essential, including RANS, DSM, ASM, and LES. RANS model is further divided based on the number of equations. The Spalart-Allmaras model is a single-equation RANS, while K-Omega and K-Epsilon are two-equation. The computational result produced by each turbulence model will vary depending on the subject object and flow characteristics [7, 8]. A previous study

conducted compared six turbulence models including RSM, $\overline{v^2f}$, SKW, K-Omega SST (Shear Stress Transport), SKE, and LRNKE [9]. The LES simulation results showed that RSM had the smallest error among the four other models, followed by the $\overline{v^2f}$, SKW, and K-Omega SST. In contrast, SKE and LRNKE produced significantly less accurate results. Argyropoulos and Markatos also explored turbulent flow, where LES provided the best computational results, offering superior visualization, including flow separation and vorticity, compared to RANS, DSM, and ASM models.

In another study on waterwheels using CFD, K-Omega SST and K-Epsilon were analysed. The results showed that K-Omega SST provided a better numerical method but required longer simulation time compared to K-Epsilon [10]. Through the turbulence model analysis on a hatchback vehicle, both DDES and SBES K-Omega SST models were found to produce relatively similar results with a lift coefficient difference of +0.005. Compared to wind tunnel measurements, the SBES K-Omega SST model showed more stable convergence [11]. The appropriate turbulence model for flow over a NACA 0012 aerofoil had also been explored. Among all models analysed, K-Epsilon provided good results that correlated with experimental data for small angles of the NACA 0012 aerofoil, without causing flow separation [12]. In the aerodynamics industry, Spalart-Allmaras model is the best turbulence model due to the partial differential equations (PDE) that are well-suited for numerical simulations with short simulation times while retaining significant turbulent flow characteristics [13].

Based on the background above, the problem statement is to determine the best turbulence model for numerical simulation of twin-floater amphibious aircraft in terms of lift and drag coefficients. This study aimed to compare and analyses three commonly used turbulence models: K-Omega SST, K-Epsilon, and Spalart-Allmaras.

2. METHODOLOGY

2.1 Geometry modelling

The main dimensions of the simulation geometry are shown in Table I. Fig. 1 shows a schematic image of the entire body of the amphibious aircraft, which is the geometric model in this simulation.

Table I: Geometry of aircraft model.

Dimension	Symbol	Prototype	Model (scale 1:6.3)
Length over all	L	17.75 m	2.65 m
Wing span	S	20.77 m	3.1 m
Angle of attack	α	-	$-10^\circ, -5^\circ, 0^\circ, 5^\circ, 10^\circ, 15^\circ, 16^\circ, 20^\circ$

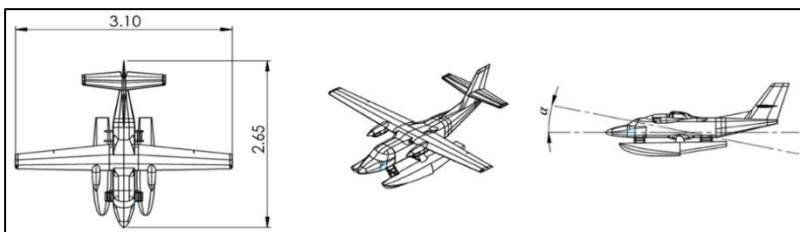


Figure 1: Geometry scheme of twin-floater amphibious aircraft model.

The computational domain in the analysis used a free-surface mode to simulate the wind tunnel accurately, as shown in Fig. 2. The total wingspan [14] determined the domain size. The inlet was positioned at twice the wingspan length in front of the aircraft. Similarly, the sides, top, and bottom were positioned at a distance of twice the wingspan length, while the outlet was placed five times the wingspan length behind.

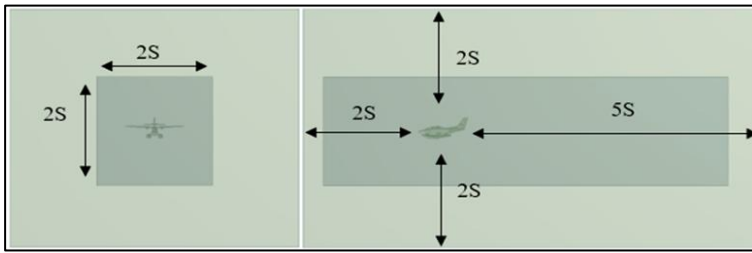
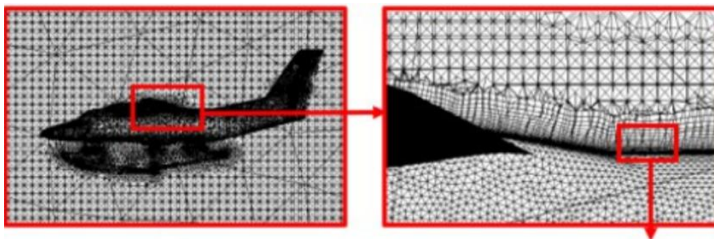


Figure 2: Geometry domain of the simulation.

The Body of Influence (BOI) was applied using a hierarchical method to identify key geometric features and areas of interest within the computational domain. This included analysing flow characteristics, such as vorticity, velocity gradients, and pressure gradients, to determine resolution accuracy. After identification, these areas were specially marked, and mesh refinement was applied to enhance resolution and capture flow features with higher accuracy. The BOI method offered adaptability and scalability, allowing users to adjust mesh refinement criteria based on specific simulation requirements and the desired level of accuracy [15, 16].

2.2 Mesh formation

The mesh method for BOI was created using software with an automatic strategy. A tetrahedral mesh configuration was selected to adapt the shape to the complex surface of aircraft. The total number of grids produced was 26 million cells and the thickness of the first boundary layer attached to the wall was $1,27 \times 10^{-6}$ m. There were 35 boundary layers near the wall, with thickness ratio of 1.3. The mesh image on the aircraft surface is shown in Fig. 3.



a) Face sizing



b) Inflation layer

Figure 3: Mesh domain for simulation.

The quality of the grid, skewness, and orthogonal quality were checked during operation. Skewness indicated the asymmetry of grid elements, and orthogonal quality measured the regularity of the angles. The maximum skewness and minimum orthogonal quality values of this mesh were found 0.9 and 0.18, respectively. Skewness and orthogonal quality were in the acceptable category based on the mesh metrics spectrum for skewness and orthogonal quality.

In addition to skewness and orthogonal quality, the y^+ mesh quality value requires attention. The y^+ is the non-dimensional distance between the first grid node and the wall surface, which is calculated using Eq. (1) [17].

$$\frac{y}{L} = \frac{y^+}{\left(Re \sqrt{\frac{C_f}{2}}\right)} \quad (1)$$

When there is flow separation near the wing surface, the quality of mesh element formation in the boundary layer area of the wing surface should be maintained at a y^+ value < 5 [18]. Fig. 4 shows the y^+ contour values on the geometry wall.

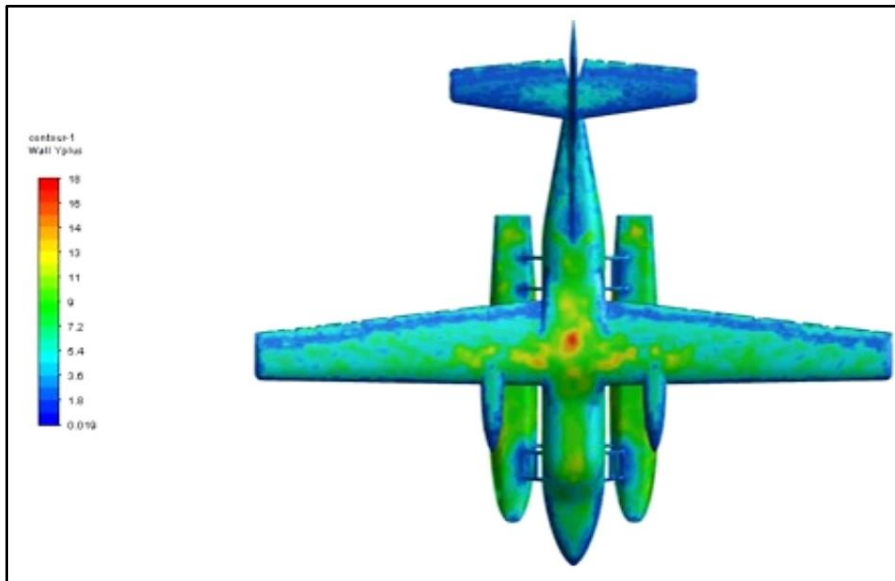


Figure 4: Contour Y^+ value.

2.3 Simulation setting and grid test

Boundary conditions, including inlet velocity, outlet pressure, and wall condition, were determined to simulate realistic airflow around the aircraft. In this case, the simulation modelling used commonly used turbulence models, namely, standard Spalart–Allmaras, K-Omega SST, and standard K-Epsilon. In this simulation test, the Semi Implicit Method for Pressure Linked Equations (SIMPLE) was used to connect the pressure and velocity fields. The Algebraic Multi-Grid solver was used to speed solution convergence using a second-order upwind discrete scheme.

This method alluded to a comparable study carried out [19]. A grid independence test compared the number of mesh elements against one of the output parameters. The results of the grid test process showed that the number of cell elements used was optimal, where the number of cells used did not significantly affect the computational results [20]. In this study, 26 million elements were used, and the error value for the grid independence test 1.84 %, with the Grid-independence test graph shown in Fig. 5. Allowable error values for Grid- independent test does not exceed 5 % [21].

2.4 Numerical simulation

This study simulated the aerodynamics of amphibious aircraft using CFD through the ANSYS Fluent program. The fundamental equations governing this computation were the continuity equation (mass conservation) and the Navier-Stokes equations, which asserted that the mass flow rate into an element equalled the rate of change in the fluid element. Specifically, the

Navier-Stokes equations represented a system of nonlinear differential equations describing fluids flow. These equations could be used to explain the balance of forces acting on fluids, including body and surface forces. ANSYS Fluent was used to solve the time-dependent, three-dimensional form of these equations, accounting for convective, diffusive, and pressure gradient terms [22].

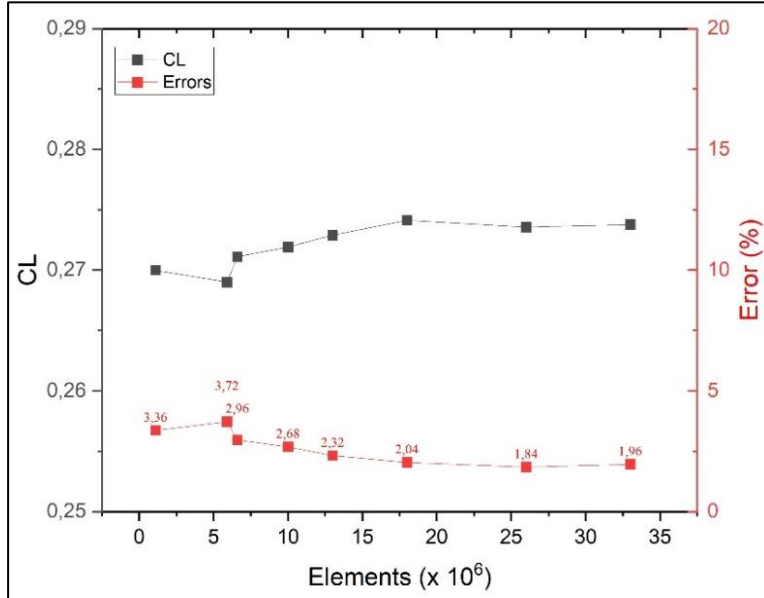


Figure 5: Grid-independent mesh.

In determining the solution to the numerical equations, the turbulence model served as a computational procedure to approximate the flow equation system and facilitate the calculation of various flow problems. Generally, turbulence models are used to modify the Navier-Stokes equations by incorporating mean and large fluctuations, leading to the Reynolds-Averaged Navier-Stokes equations. The RANS equations are shown in Eqs. (2) and (3) [23].

$$\frac{\partial \rho}{\partial t} + \frac{\partial \bar{u}_i}{\partial x_i} = 0 \quad (2)$$

$$\frac{\partial}{\partial t} (\rho \bar{u}_i) + \frac{\partial}{\partial x_j} (\rho \bar{u}'_i \bar{u}'_j) = -\frac{\partial \bar{P}}{\partial x_j} + \frac{\partial}{\partial x_j} \left(\mu \left(\frac{\partial \bar{u}_i}{\partial x_j} + \frac{\partial \bar{u}_j}{\partial x_i} \right) \right) - (\rho \bar{u}'_i \bar{u}'_j) + g_i \quad (3)$$

where x_i and x_j are coordinates, \bar{u}_i and \bar{u}_j represent the mean velocity components, \bar{P} is the mean pressure, ρ is density, g_i is the acceleration due to gravity along the inertia coordinate axis, μ represents the effective viscosity coefficient of dynamic viscosity, and $(\rho \bar{u}'_i \bar{u}'_j)$ is the Reynolds stress.

In conducting CFD, there is a need to consider how the flow properties change in specific regions (x, y, z). The basic Eulerian theory is used to apply the control volume in describing fluid motion. The fluid velocity at a point can be mathematically represented using a vector that is a function of space and time with the following Eqs. (4) and (5).

$$\vec{V} = \vec{V}(x, y, z, t) \quad (4)$$

$$\frac{\partial \rho}{\partial t} + \vec{\nabla}(\rho \vec{V}) = 0 \quad (5)$$

Spalart-Allmaras model is a single-equation turbulence model that solves the transport equation for turbulent kinematic viscosity. This model can be used in relatively coarse simulations with large mesh sizes, where detailed turbulent flow calculations are not critical. Moreover, accurate modelling near the wall is important to estimate pressure drop and flow

separation, as boundary layer depends on accurate predictions of the local wall shear force. This shows the need for additional treatment to more accurately predict flow behaviour near the wall, particularly in wall-affected flows. Spalart-Allmaras turbulence model can be formulated in the following Eq. (6) [23].

$$\frac{\partial}{\partial t}(\rho \tilde{v}) + \frac{\partial}{\partial x_i}(\rho \tilde{v} u_i) = G_v + \frac{1}{\sigma_{\tilde{v}}} \left[\frac{\partial}{\partial x_j} \left((\mu + \rho \tilde{v}) \frac{\partial \tilde{v}}{\partial x_j} \right) + c_{b2} \rho \left(\frac{\partial \tilde{v}}{\partial x_j} \right)^2 \right] - Y_v + S_{\tilde{v}} \quad (6)$$

where G_v is the creation of turbulent viscosity, Y_v is the destruction of turbulent viscosity in the near-wall area owing to wall blocking and viscous damping, \tilde{v} is the kinematic viscosity of the molecular fluid, and $S_{\tilde{v}}$ is a user-defined source.

K-Epsilon model is a semi-empirical model created by Launder & Spalding. This model is fairly thorough, with two equations that allow for the independent calculation of turbulent velocity and length scales. Additionally, it is widely used in fluid and heat transfer simulations due to stability, computational efficiency, and appropriate accuracy for a variety of turbulent flows. The conventional type depends on transport equations for turbulent kinetic energy (k) and dissipation rate (ε). K-Epsilon turbulence model is expressed in the following two Eqs. (7) and (8) [23].

$$\frac{\partial}{\partial t}(\rho k) + \frac{\partial}{\partial x_i}(\rho k u_i) = \frac{\partial}{\partial x_j} \left[\left(\mu + \frac{\mu_t}{\sigma_k} \right) \frac{\partial k}{\partial x_j} \right] + G_k + G_b - \rho \varepsilon - Y_M + S_k \quad (7)$$

$$\frac{\partial}{\partial t}(\rho \varepsilon) + \frac{\partial}{\partial x_i}(\rho \varepsilon u_i) = \frac{\partial}{\partial x_j} \left[\left(\mu + \frac{\mu_t}{\sigma_\varepsilon} \right) \frac{\partial \varepsilon}{\partial x_j} \right] + C_{1\varepsilon} \frac{\varepsilon}{k} (G_k + C_{3\varepsilon} G_b) - C_{2\varepsilon} \rho \frac{\varepsilon^2}{k} + S_\varepsilon \quad (8)$$

where G_k represent the turbulent kinetic energy from mean velocity gradient, G_b is the buoyancy turbulent kinetic energy, Y_M is the contribution in fluctuating dilatation to compressible turbulent flow dissipation, C_{1s} , C_{2s} , C_{3s} are constants, σ_k , σ_s represent the Prandtl numbers for k and ε , and S_k , S_s are energy sources determined

The standard K-Omega model is a turbulence model based on Wilcox's K-Omega model but with various changes to account for low Reynolds number flow effects, compressibility, and shear flow dispersion. This model can be used to both internal channel and free shear flows. The classic K-Omega model uses empirical transport equations to calculate turbulent kinetic energy (k) and specific dissipation rate (ω), also known as the ε - k ratio. Moreover, K-Omega turbulence model is formulated in the following two Eqs. (9) and (10) [5, 13].

$$\frac{\partial}{\partial t}(\rho k) + \frac{\partial}{\partial x_j}(\rho k u_j) = \frac{\partial}{\partial x_j} \left(\Gamma_k \frac{\partial k}{\partial x_j} \right) + G_k - Y_k \quad (9)$$

$$\frac{\partial}{\partial t}(\rho \omega) + \frac{\partial}{\partial x_j}(\rho \omega u_j) = \frac{\partial}{\partial x_j} \left(\Gamma_\omega \frac{\partial \omega}{\partial x_j} \right) + G_\omega - Y_\omega \quad (10)$$

where G_ω and G_k are the generation of ω and k respectively, Γ_ω and Γ_k are the effective diffusivity of ω and k respectively. Y_ω and Y_k are the dissipation of ω and k in the turbulence respectively.

One of the most challenging aspects of turbulence modelling was found to be accurate prediction of flow separation on smooth surfaces. Eqs. (8) and (9) frequently failed to appropriately predict the onset location and extent of flow separation under adverse pressure gradient circumstances. This was a major occurrence in various technical applications, particularly in aircraft aerodynamics, where stall characteristics are determined by flow separation on the wings. Therefore, a more accurate model for predicting flow separation was created. The SST model was used to provide high precision in beginning the location and flow separation under unfavourable pressure gradients by including transport effects into the eddy viscosity formulation. This model was recommended for accurately simulating boundary layers, thereby requiring high resolution in the boundary layer. The advantage of the SST model

included the ability to predict flow separation more accurately, suitability for high precision in the boundary layer, accurate handling of near-wall treatment calculations at low Reynolds numbers. Despite the advantages, the SST model showed some drawbacks, requiring a high-quality and dense grid around the walls, as well as greater effort during simulation pre-processing. The transport equations for the SST turbulence model are shown in Eq. (11) [5].

$$\frac{\partial(\rho\gamma)}{\partial t} + \frac{\partial(\rho U_j \gamma)}{\partial x_j} = P_{\gamma 1} - E_{\gamma 1} + P_{\gamma 2} + \frac{\partial}{\partial x_j} \left[\left(\mu + \frac{\mu_t}{\sigma_\gamma} \right) \frac{\partial \gamma}{\partial x_j} \right] \quad (11)$$

where γ is intermittency, $P_{\gamma 1}$ and $E_{\gamma 1}$ are transition sources, $P_{\gamma 2}$ and $E_{\gamma 2}$ are destruction/reclamation sources.

2.5 Experiment wind tunnel

Wind tunnel experiment is a reliable method for obtaining accurate data and precise insights into wind flow characteristics around an object [7]. In this study, validation was performed using experimental results from subsonic wind tunnel testing in a closed-circuit configuration to obtain lift and drag coefficient measurements for a twin-floaters amphibious aircraft [24]. Wind Tunnel Test Section shown in Fig. 6.

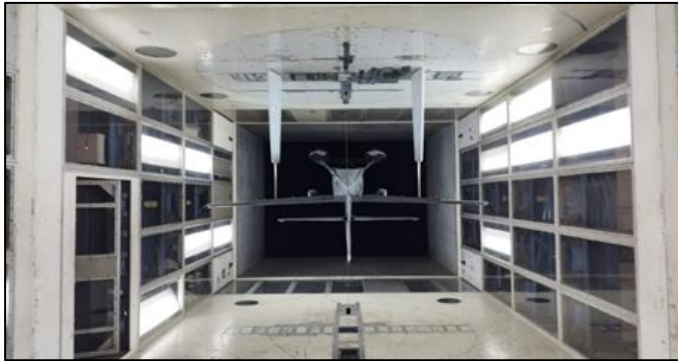


Figure 6: Wind tunnel test section.

The test section of the wind tunnel has dimensions of 4 m × 3 m × 2 m (length × width × height), with an operational wind tunnel speed of 65 m/s. Manufacturing and assembly of the wind tunnel model have a maximum dimensional error of 80 microns. Due to the absence of low visualization experiment, CFD simulation is used to determine the flow characteristics simulation and analyses of the Twin-floater of the amphibian aircraft in the wind tunnel test dataset.

2.6 Validation

Validation study was conducted to compare simulation results with experimental data or analytical solutions, showing the accuracy of computational values. Simulation resources, including hardware specifications and processing time, were determined to provide a comprehensive overview of the study computational framework.

3. RESULTS AND DISSCUSION

3.1 Effect of turbulence model evaluated by pressure gradient and pathline velocity

NASA states that the Bernoulli effect explains how the difference in airspeed above and below the wing creates a pressure difference. According to Newton's Laws, the air deflected downward by the wing generates an upward reaction force (lift). Therefore, an aircraft can fly due to pressure differences (Bernoulli) and changes in air momentum (Newton's law). Lift can

be generated based on Newton's third law of action and reaction. An opposite reaction occurs as the air is deflected downward, creating an upward lift force.

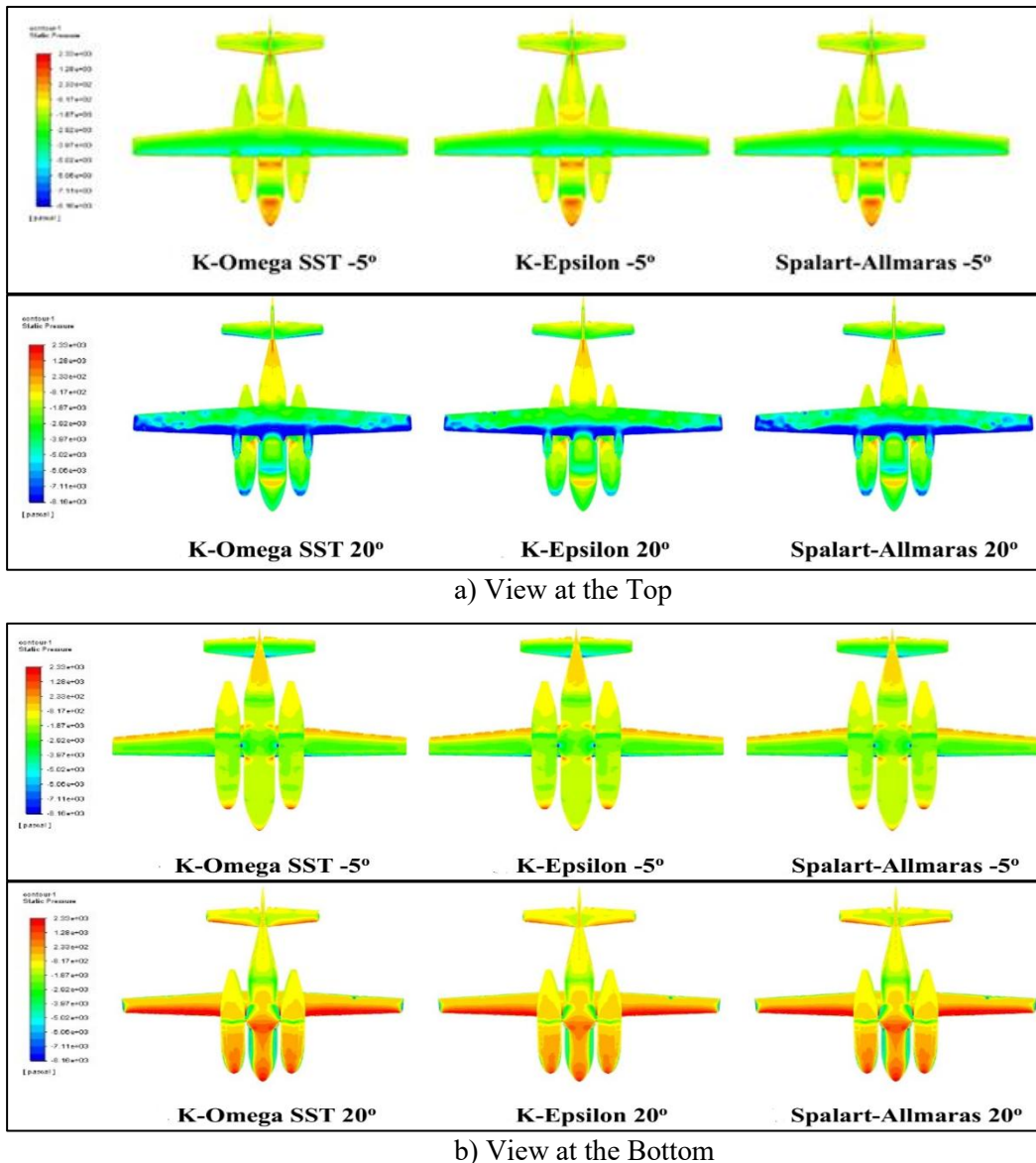


Figure 7: Pressure gradient of twin-floater amphibious aircraft.

The pressure differences in Fig. 7 show the gradient distribution on the upper and lower surfaces of the twin-floater amphibious aircraft. The pressure gradient of the twin-floater amphibious aircraft was found at 65 m/s, where each viscous model showed relatively similar contours. This result showed that lift coefficients also had a range of results not significantly different. In terms of pressure gradient patterns, all three models showed similar increases in values, but K-Omega SST produced more accurate values compared to K-epsilon and Spalart-Allmaras. Similarly, in waterwheel simulation [25], showed that K-Omega SST provided results in line with experimental data. Also stated that the use of K-Omega SST showed excellent results [26].

Fig. 7 showed that the pressure at the front of the twin-floater amphibious aircraft was higher due to direct contact with incoming airflow. This interaction created pressure gradients above and below the wings due to the formation of small vortices, as visible in Fig. 7 b.

Fig. 8 is a visualization of flow separation, where separation is above the aircraft's wing. At low inclination angles ranging from -5° to 5° angle of attack, all three turbulence model

variations showed similar results in flow separation. However, at extreme attack angles such as 20° , clear differences in flow separation were observed. Spalart-Allmaras visualized flow separation and turbulence more distinctly compared to K-Omega SST and K-Epsilon models [27].

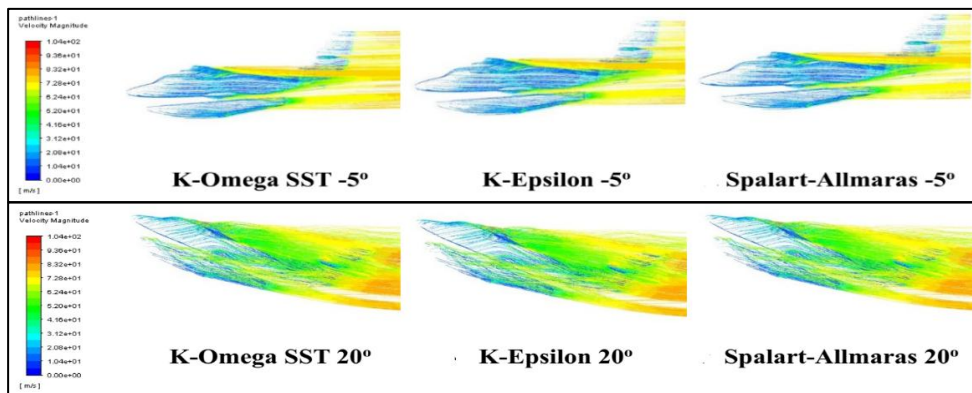


Figure 8: Pathline velocity of twin-floater amphibious aircraft.

3.2 Effect of turbulence models assessed by generated vorticity

Based on the results of flow visualization simulations as shown in Fig. 9, Spalart-Allmaras was able to capture vorticity more distinctly.

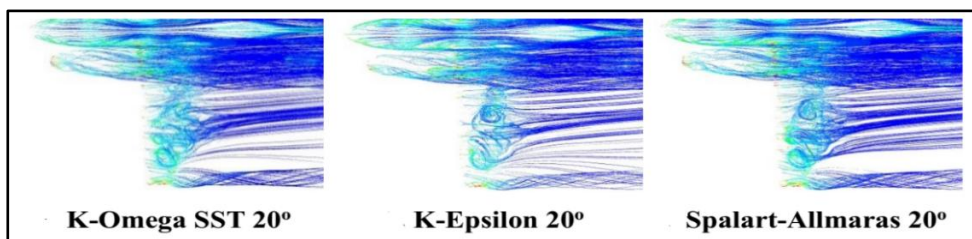


Figure 9: Vorticity of twin-floater amphibious aircraft.

For K-Epsilon and K-Omega SST, the visualization results showed vorticity levels lower than Spalart-Allmaras model. This difference was because Spalart-Allmaras model directly solved the transport equation for eddy viscosity vortex [28, 29]. Additionally, Spalart-Allmaras model performed well in the wake area where vorticity dominated the strain rate. This showed the potential to handle eddy viscosity production more effectively compared to K-Epsilon model [30].

3.3 Effect of turbulence model assessed by C_L and C_D produced

To examine the additional effects of twin-floaters, the aerodynamic coefficients must be evaluated at various angles of attack, considering the stall angle where aircraft loses lift. In analysing these aerodynamic characteristics, there is a need to review the lift coefficient and drag coefficient of the aircraft at take-off, cruise, and landing angles [30].

Validation in this study was conducted by comparing the lift coefficient values from the simulation with the experiments [24]. The comparison between the simulation and experimental results at seven points of angle of attack are shown in Fig. 10. Based on the results, at extreme angles of attack such as -10° and above 15° , K-Epsilon performed poorly with the largest error of 40% achieved as -10° . In comparison, Spalart-Allmaras with an average error of 7.2%, provided results with minimal fluctuation and a better average error K-Epsilon. K-Omega SST model showed excellent results, while Standard K-Epsilon had a larger deviation. The overall difference between the results was below 5%, with an average error of 3.77%.

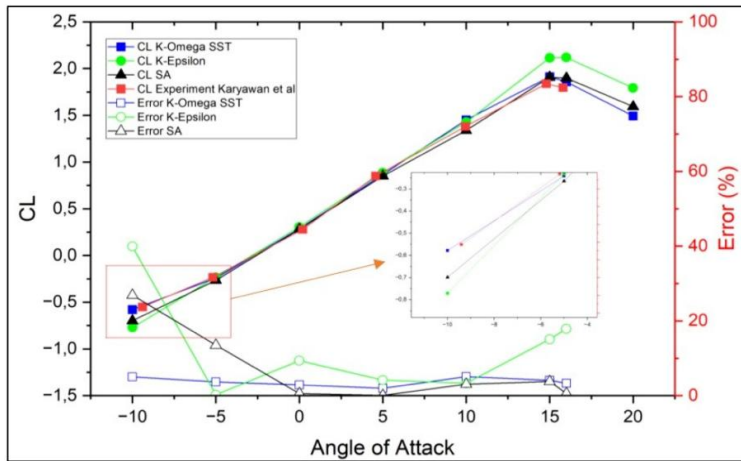


Figure 10: Validation experiment.

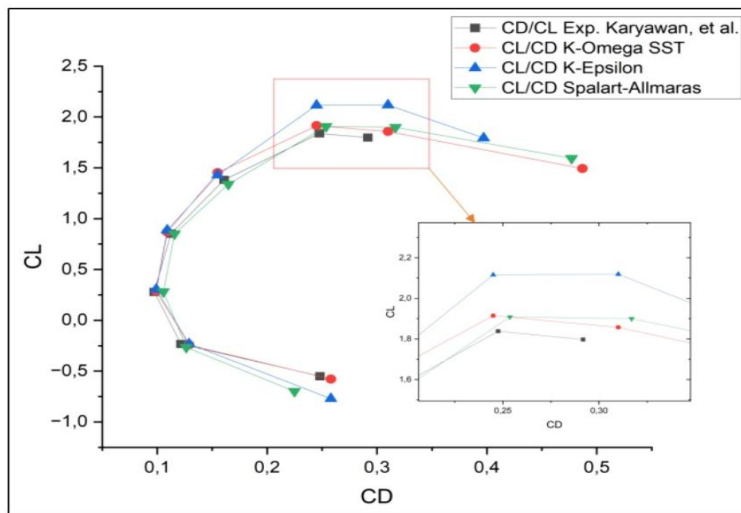


Figure 11: C_L/C_D graph on each turbulence model.

Based on the C_L/C_D graph in Fig. 11, all three turbulence models have low error values at angles of attack -5° , 0° , and 5° . At higher angles of attack such as 15° and 16° , K-Epsilon shows significantly higher errors compared to others.

The maximum C_L/C_D ratio represented the glide ratio. The experimental results [16] were observed in the zoomed-in box, which showed a C_L/C_D maximum value of 8.529. The calculations using K-Omega SST and K-Epsilon models obtained higher values of 9.367 and 9.208, respectively. In comparison, Spalart-Allmaras model produced lower values but was closer to the experimental results of 8,132 with an error of 5.05 %. This was possible because K-Omega SST proposed by Wilcox could predict turbulence by solving two equations for two additional variables, namely turbulent kinetic energy (k) and specific dissipation rate (ω). The method combined K-Omega and K-Epsilon models, which performed better for cases near walls, particularly under adverse pressure gradients [31].

4. CONCLUSION

The best turbulence model from the results of computing and C_L/C_D calculating for the amphibious aircraft model without a propeller has the Spalart-Allmaras model with a lower value, and the error results are less than 5.05 %.

The future research will evaluate the effectiveness of the ratio of inter pontoon spacing to total pontoon length (S/L). design with propeller using numerical and experimental synthesis

approaches yielded important findings regarding drag characteristics, stability, and hydro-aero dynamic.

ACKNOWLEDGEMENT

This study is a collaboration between the National Research and Innovation Agency (BRIN), Hang Tuah University, and Diponegoro University. The authors are grateful to the Education Fund Management Institute (LPDP) of the Ministry of Finance for funding this study through the Research and Innovation Funding Program for Advanced Indonesia (RIIM), which was led by Dr. Ir. Sayuti Syamsuar, M.T.

REFERENCES

- [1] Cribb, R.; Ford, M. (2009). Indonesia as an Archipelago: Managing Islands, Managing the Seas, Cribb, R.; Ford, M. (Eds.), *Indonesia Beyond the Water's Edge: Managing an Archipelagic State*, ISEAS Publishing, Singapore, 1-27
- [2] Karyawan, K.; Suwasono, B.; Sutiyo, S.; Syamsuar, S.; Fadjar, R.; Triputra, F. R.; Pane, I. Z.; Haryanto, I.; Tauviqirrahman, M.; Yohana, E. (2024). Hydrodynamic characteristics for catamaran floatplane in taxiing conditions, *International Review of Aerospace Engineering*, Vol. 17, No. 1, 1-11, doi:[10.15866/irease.v17i1.24489](https://doi.org/10.15866/irease.v17i1.24489)
- [3] Culberson, S. D. (2011). Environmental Impacts of Airports, Ashford, N. J.; Mumayiz, S. A.; Wright, P. H. (Eds.), *Airport Engineering: Planning, Design, and Development of 21st Century Airports*, 4th Edition, Wiley, Hoboken, 704-738
- [4] Wang, H.; Zhu, R.; Zha, L.; Gu, M. (2022). Experimental and numerical investigation on the resistance characteristics of a high-speed planing catamaran in calm water, *Ocean Engineering*, Vol. 258, Paper 111837, 18 pages, doi:[10.1016/j.oceaneng.2022.111837](https://doi.org/10.1016/j.oceaneng.2022.111837)
- [5] Wilcox, D. C. (1988). Multiscale model for turbulent flows, *American Institute of Aeronautics and Astronautics Journal*, Vol. 26, No. 11, 1311-1320, doi:[10.2514/3.10042](https://doi.org/10.2514/3.10042)
- [6] Daneshjoo, N.; Mares, A.; Malega, P.; Francova, Z. (2022). CAD model of rear-view mirror and simulation of its aerodynamics and noise, *International Journal of Simulation Modelling*, Vol. 21, No. 2, 226-236, doi:[10.2507/IJSIMM21-2-598](https://doi.org/10.2507/IJSIMM21-2-598)
- [7] Kosutova, K.; Vanderwel, C.; van Hooff, T.; Blocken, B.; Hensen, J. L. M. (2024). Wind-tunnel experiments on cross-ventilative cooling in a generic isolated building with one heated wall: impact of opening size, *Building and Environment*, Vol. 259, Paper 111628, 17 pages, doi:[10.1016/j.buildenv.2024.111628](https://doi.org/10.1016/j.buildenv.2024.111628)
- [8] Wang, J.; Zhang, J. R.; Liu, X. L. (2025). CFD simulation of wind-rain effects on ultra-high-speed train aerodynamics and safety, *International Journal of Simulation Modelling*, Vol. 24, No. 4, 706-717, doi:[10.2507/IJSIMM24-4-CO18](https://doi.org/10.2507/IJSIMM24-4-CO18)
- [9] El-Behery, S. M.; Hamed, M. H. (2011). A comparative study of turbulence models performance for separating flow in a planar asymmetric diffuser, *Computers & Fluids*, Vol. 44, No. 1, 248-257, doi:[10.1016/j.compfluid.2011.01.009](https://doi.org/10.1016/j.compfluid.2011.01.009)
- [10] Argyropoulos, C. D.; Markatos, N. C. (2015). Recent advances on the numerical modelling of turbulent flows, *Applied Mathematical Modelling*, Vol. 39, No. 2, 693-732, doi:[10.1016/j.apm.2014.07.001](https://doi.org/10.1016/j.apm.2014.07.001)
- [11] Buscariolo, F. F.; Magazoni, F.; Wolf, M.; Maruyama, F. K.; Alves, J. C. L.; Della Volpe, L. J. (2016). Analysis of turbulence models applied to CFD drag simulations of a small hatchback vehicle, *25th SAE BRASIL International Congress and Display*, doi:[10.4271/2016-36-0201](https://doi.org/10.4271/2016-36-0201)
- [12] Rhie, C. M.; Chow, W. L. (1983). Numerical study of the turbulent flow past an airfoil with trailing edge separation, *American Institute of Aeronautics and Astronautics Journal*, Vol. 21, No. 11, 1525-1532, doi:[10.2514/3.8284](https://doi.org/10.2514/3.8284)
- [13] Bueno-Orovio, A.; Castro, C.; Palacios, F.; Zuazua, E. (2012). Continuous adjoint approach for the Spalart-Allmaras model in aerodynamic optimization, *American Institute of Aeronautics and Astronautics Journal*, Vol. 50, No. 3, 631-646, doi:[10.2514/1.J051307](https://doi.org/10.2514/1.J051307)
- [14] Morden, J. A.; Hemida, H.; Baker, C. J. (2015). Comparison of RANS and detached eddy simulation results to wind-tunnel data for the surface pressures upon a class 43 high speed train, *Journal of Fluids Engineering*, Vol. 137, No. 4, Paper 041108, 9 pages, doi:[10.1115/1.4029261](https://doi.org/10.1115/1.4029261)

- [15] Karkoulias, D. G.; Tzoganis, E. D.; Panagiotopoulos, A. G.; Acheimastos, S.-G. D.; Margaritis, D. P. (2022). Computational fluid dynamics study of wing in air flow and air–solid flow using three different meshing techniques and comparison with experimental results in wind tunnel, *Computation*, Vol. 10, No. 3, Paper 34, 24 pages, doi:[10.3390/computation10030034](https://doi.org/10.3390/computation10030034)
- [16] Wang, Y.; Zhu, Q.; Huang, T.; Han, X.; Lin, M. (2024). Modelling and simulation of nonlinear dynamic flow field and temperature field of depyrogeneration tunnel, *Facta Universitatis, Series: Mechanical Engineering*, Vol. 22, No. 1, 45-62, doi:[10.22190/FUME221221011W](https://doi.org/10.22190/FUME221221011W)
- [17] Montoya, M. C.; Nieto, F.; Alvarez, A. J.; Hernandez, S.; Jurado, J. A.; Sánchez, R. (2018). Numerical simulations of the aerodynamic response of circular segments with different corner angles by means of 2D URANS. Impact of turbulence modelling approaches, *Engineering Applications of Computational Fluid Mechanics*, Vol. 12, No. 1, 750-779, doi:[10.1080/19942060.2018.1520741](https://doi.org/10.1080/19942060.2018.1520741)
- [18] Fouatih, O. M.; Imine, B.; Medale, M. (2019). Numerical/experimental investigations on reducing drag penalty of passive vortex generators on a NACA 4415 airfoil, *Wind Energy*, Vol. 22, No. 7, 1003-1017, doi:[10.1002/we.2330](https://doi.org/10.1002/we.2330)
- [19] Tang, Y.; Guo, B.; Ranjan, D. (2015). Numerical simulation of aerosol deposition from turbulent flows using three-dimensional RANS and LES turbulence models, *Engineering Applications of Computational Fluid Mechanics*, Vol. 9, No. 1, 174-186, doi:[10.1080/19942060.2015.1004818](https://doi.org/10.1080/19942060.2015.1004818)
- [20] Yemenici, O.; Oruc, E. (2025). Aerodynamic and structural analysis of a solar panel, *International Journal of Simulation Modelling*, Vol. 24, No. 2, 191-202, doi:[10.2507/IJSIMM24-2-709](https://doi.org/10.2507/IJSIMM24-2-709)
- [21] Lee, M.; Park, G.; Park, C.; Kim, C. (2020). Improvement of grid independence test for computational fluid dynamics model of building based on grid resolution, *Advances in Civil Engineering*, Vol. 2020, Paper 8827936, 11 pages, doi:[10.1155/2020/8827936](https://doi.org/10.1155/2020/8827936)
- [22] Özel, M. A.; Kopmaz, O. (2024). Design of a periodic structure for composite helicopter rotor blade, *International Journal of Simulation Modelling*, Vol. 23, No. 3, 447-458, doi:[10.2507/IJSIMM23-3-692](https://doi.org/10.2507/IJSIMM23-3-692)
- [23] Sulistiya, S.; Kasman, A. S. (2018). The turbulence model validation in numerical simulation using Fluent software with the wing of ONERA M6, *Journal of Aero Technology*, Vol. 2, No. 1, 19-25, doi:[10.29122/joat.v2i1.3817](https://doi.org/10.29122/joat.v2i1.3817)
- [24] Karyawan, K.; Suwasono, B.; Supartono, S.; Syamsuar, S.; Muharam, A.; Widyawasta, W.; Pane, I. Z.; Haryanto, I.; Tauviqirrahman, M.; Yohana, E. (2024). Dataset of the twin floater of amphibian aircraft in wind tunnel test, *Data in Brief*, Vol. 57, Paper 111008, 15 pages, doi:[10.1016/j.dib.2024.111008](https://doi.org/10.1016/j.dib.2024.111008)
- [25] Adanta, D.; Fattah, I. M. R.; Muhammad, N. M. (2020). Comparison of standard k-epsilon and SST k-omega turbulence model for breastshot waterwheel simulation, *Journal of Mechanical Science and Engineering*. Vol. 7, No. 2, 39-44, doi:[10.36706/jmse.v7i2.44](https://doi.org/10.36706/jmse.v7i2.44)
- [26] Kusuma, Y. F.; Sulistiya, S.; Hendrato, H.; Muhammad, M.; Halfina, B.; Ansori, I.; Kurniawan, A. D.; Verma, G.; Priatno, D. H.; Fuad, A. P.; Syamsuar, S.; Karyawan, K.; Widyawasta, W. (2024). The effect of floater shape on amphibious aircraft's drag coefficient using computational fluid dynamics method, *International Review of Aerospace Engineering*, Vol. 17, No. 2, 50-59, doi:[10.15866/irease.v17i2.24747](https://doi.org/10.15866/irease.v17i2.24747)
- [27] Marciotto, E. R. (2016). Classic Bernoulli's principle derivation and its working hypotheses, *Physics Education*, Vol. 51, No. 4, Paper 045005, 6 pages, doi:[10.1088/0031-9120/51/4/045005](https://doi.org/10.1088/0031-9120/51/4/045005)
- [28] Taleghani, A. S.; Ghajar, A. (2024). Aerodynamic characteristics of a delta wing aircraft under ground effect, *Frontiers in Mechanical Engineering*, Vol. 10, Paper 1355711, 16 pages, doi:[10.3389/fmech.2024.1355711](https://doi.org/10.3389/fmech.2024.1355711)
- [29] Diskin, B.; Liu, Y.; Galbraith, M. C. (2023). High-Fidelity CFD Verification Workshop 2024: Spalart-Allmaras QCR2020 turbulence model, *AIAA SCITECH Forum*, doi:[10.2514/6.2023-1244](https://doi.org/10.2514/6.2023-1244)
- [30] Kostić, Č. (2015). Review of the Spalart-Allmaras turbulence model and its modifications to three-dimensional supersonic configurations, *Science Technical Review*, Vol. 65, No. 1, 43-49, doi:[10.5937/STR1501043K](https://doi.org/10.5937/STR1501043K)
- [31] Yan, Y.; Avital, E.; Williams, J.; Cui, J. (2019). CFD analysis for the performance of micro-vortex generator on aerofoil and vertical axis turbine, *Journal of Renewable and Sustainable Energy*, Vol. 11, No. 4, Paper 043302, 33 pages, doi:[10.1063/1.5110422](https://doi.org/10.1063/1.5110422)